

Electrochemical Activation Applied to Perovskite Titanate Fibers to Yield Supported Alloy Nanoparticles for Electrocatalytic Application

Min Xu, Chencheng Liu, Aaron B. Naden, Herbert Früchtl, Michael Bühl, and John T. S. Irvine*

Active bi-metallic nanoparticles are of key importance in catalysis and renewable energy. Here, the in situ formation of bi-metallic nanoparticles is investigated by exsolution on 200 nm diameter perovskite fibers. The B-site co-doped perovskite fibers display a high degree of exsolution, decorated with NiCo or Ni₃Fe bi-metallic nanoparticles with average diameter about 29 and 35 nm, respectively. The perovskite fibers are utilized as cathode materials in pure CO₂ electrolysis cells due to their redox stability in the CO/CO₂ atmosphere. After in situ electrochemical switching, the nanoparticles exsolved from the perovskite fiber demonstrate an enhanced performance in pure CO₂ electrolysis. At 900 °C, the current density of solid oxide electrolysis cell (SOEC) with 200 μm YSZ electrolyte supported NiFe doped perovskite fiber anode reaches 0.75 Acm⁻² at 1.6 V superior to the NiCo doped perovskite fiber anode (about 1.5 times) in pure CO₂. According to DFT calculations (PBE-D3 level) the superior CO₂ conversion on NiFe compared to NiCo bi-metallic species is related to an enhanced driving force for C-O cleavage under formation of CO chemisorbed on the nanoparticle and a reduced binding energy of CO required to release this product.

1. Introduction

The ever-increasing CO₂ emission into the atmosphere is thought as the primary reason for the global warming during the past century. Development of carbon capture and storage techniques can play a role in tackling this problem in a sustainable way. An alternative to storage is the use of CO₂ as feedstock for high-value products. A technology that has attracted widespread attention in that respect is the use of SOECs.^[1–3] SOECs convert electricity into chemical energy using electrochemical

catalysis, with the cathode usually working in CO₂ or CO₂/H₂O. Thus, the cathode materials for SOECs have to fulfill requirements such as being able to work in an oxygen partial pressure (p_{O_2}) higher than that of H₂ but lower than that of air.^[4] In principle, cermet Ni-YSZ electrodes can be used as cathode for CO₂ electrolysis but they suffer from high overpotential for CO oxidation and limited redox stability in CO/CO₂ environments. Therefore, traditional deposition and infiltration have been widely used to prepare highly active catalysts for CO₂ SOEC but have typically been limited by the anchorage of synthesized species, size, and distribution of nanoparticles.^[5,6] Exsolution has been widely employed to produce heterogeneous catalysts with nanoparticles (NPs) supported on parent materials. This time- and cost-effective method has been successfully utilized to form various transition metal nanoparticles, including

noble metals^[7–9] and first-row transition metals.^[10–12] Monometallic nanoparticles exsolved on the host materials have been extensively applied in various chemical and energy conversion processes.^[13–15] The finely dispersed nanoparticles possess excellent catalytic activities and most importantly, their unique anchored structure on host materials was reported to improve their stability significantly under harsh conditions.

However, the exsolution of transition metal cations with mixed-valence has been rarely reported because of their low reducibility and high segregation energy. Consequently, sluggish exsolution happened in titanates doped with those cations, for instance, Fe and Mn.^[11,16] The segregation of Fe nanoparticles has been reported only in Fe abundant materials, such as Pr_{0.4}Sr_{0.6}Co_{0.2}Fe_{0.7}Nb_{0.1}O_{3-δ},^[17] La_{0.3}Sr_{0.7}Cr_{0.3}Fe_{0.6}Co_{0.1}O_{3-δ},^[18] and Sr₂FeMo_{0.65}Ni_{0.35}O_{6-δ}.^[19] An alternative way to produce the Fe containing nanoparticles is by introducing co-dopants to facilitate the exsolution. Bi-metallic nanoparticles formed for those situations due to the co-segregation effect of secondary dopants, such as Ni^[20] and Co.^[21] Moreover, the bi-metallic catalysts based on those transition metals display synergetic effects on promoting catalytic selectivity and activity.^[22] The exsolved bi-metallic nanoparticles were also reported to enhance the performance of materials, including catalytic reactivity,^[23] electrical

M. Xu, C. Liu, A. B. Naden, H. Früchtl, M. Bühl, J. T. S. Irvine
School of Chemistry
University of St Andrews
St Andrews KY16 9ST, UK
E-mail: jtsi@st-andrews.ac.uk

 The ORCID identification number(s) for the author(s) of this article can be found under <https://doi.org/10.1002/smll.202204682>.

© 2022 The Authors. Small published by Wiley-VCH GmbH. This is an open access article under the terms of the Creative Commons Attribution License, which permits use, distribution and reproduction in any medium, provided the original work is properly cited.

DOI: 10.1002/smll.202204682

conductivity,^[24] electrochemical activity,^[25] and CO₂ electrolysis kinetics.^[26,27] Besides, the exsolution was extensively investigated on bulk structure but rarely on the materials with high exposed surfaces, for example, fiber structure. The fiber materials bringing forth exceptional catalytic performance due to their interwoven architecture, furthermore, the 1D provide an unique platform to study the exsolution in perovskite.^[28,29]

In this work, we study the co-exsolution process of bi-metallic particles, demonstrating their application in CO₂ electrolysis. We found that the bi-metallic nanoparticles exsolved on perovskite fibers show a promising performance when used as electrode material for CO₂ SOECs. This work compared two transition metals co-dopant on the B-site perovskites, including La_{0.52}Ca_{0.28}Ni_{0.04}Fe_{0.04}Ti_{0.92}O₃ and La_{0.52}Ca_{0.28}Ni_{0.03}Co_{0.03}Ti_{0.94}O₃, hereafter denoted as LCNFT and LCNCT, respectively. The A-site defect regulation is retained at 20% for those compositions to achieve oxygen stoichiometry. The results demonstrate that the perovskite fiber electrode is very efficient for electrochemical reduction of pure CO₂.

2. Results and Discussion

2.1. Phase Analysis and Reducibility

The compositions La_{0.52}Ca_{0.28}Ni_{0.04}Fe_{0.04}Ti_{0.92}O₃ and La_{0.52}Ca_{0.28}Ni_{0.03}Co_{0.03}Ti_{0.94}O₃ were designed to keep the oxygen stoichiometry of 3 based on the anticipated oxidation states for the dopants. Keeping a total A-site occupation of 0.8, the ratio of La to Ca were adjusted in accord with the cations on the B-site. All pristine fibers were calcined at 1100 °C in the air to achieve stable crystallization phases. The XRD patterns show that both samples adopt tetragonal structures (Figure 1a). The cell parameters calculated from the Rietveld refinement are consistent with this observation (Figure S1 and Table S1, Supporting Information). The constant unit cell size is attributed to the small doping amount and the similar radius of Co³⁺ (0.61 Å), Fe³⁺ (0.645 Å), and Ni²⁺ (0.69 Å). The XRD patterns of Fe doped samples also show additional weak peaks, especially visible in the 2θ range 25–30° (Figure 1a, in the magnified range). Those reflections are assigned to oxygen-rich intergrowth species that are not randomly distributed.^[30,31] However, those intergrowth peaks are not present in La_{0.52}Ca_{0.28}Ni_{0.03}Co_{0.03}Ti_{0.94}O₃ fibers, which is possibly related to the formation of more ilmenite phases (Figure 1a). The metastable ilmenites, NiTiO₃ and CoTiO₃, may form at calcination below 1400 °C.^[32] The smaller radius of Co³⁺ may facilitate the dissolution of doped cations into the perovskite lattice. Thus, more ilmenites may form in the La_{0.52}Ca_{0.28}Ni_{0.03}Co_{0.03}Ti_{0.94}O₃ sample.

The calcined bi-metal cations doped fibers were reduced in a 5% H₂/N₂ atmosphere at 800 °C. The clear color change of the fibers indicates a reduction of the perovskite, as the light yellow samples all turn into grey. Comparing the XRD patterns, one can see that the reflections shift to lower angles for reduced samples (Figure 1a). Those shifts imply lattice expansion for the reduced samples due to B-site cation reduction/exsolution and the loss of lattice oxygen. Metallic phases can be detected from the XRD after reduction (Figure 1a, the inset). The peak at 44.5° for La_{0.52}Ca_{0.28}Ni_{0.04}Fe_{0.04}Ti_{0.92}O₃ fibers (about 44.5°)

is different from the reflections of bi-metallic phases that are corresponding to the Fe signal from the steel holder. To avoid the overlap between reflections of steel holder and bi-metallic phases, the zero-background Si substrate was used for the reduced samples.

It is known that nickel and iron can form intermetallic phases with various ratios with slight lattice parameter difference.^[33] The reflection corresponds to metallic phases for La_{0.52}Ca_{0.28}Ni_{0.04}Fe_{0.04}Ti_{0.92}O₃ sample at 44.2° indicating a composition of Ni: Fe = 3:1 that is consistent with previous reports.^[24,34] Detailed composition analysis of exsolved NiFe particles by EDX profiles will be further evaluated later. The reflection corresponding to the bi-metallic phase for the reduced La_{0.52}Ca_{0.28}Ni_{0.03}Co_{0.03}Ti_{0.94}O₃ fibers is located at 44.4° that is different from the reduced La_{0.52}Ca_{0.28}Ni_{0.04}Fe_{0.04}Ti_{0.92}O₃ sample (Figure 1a, the inset). The peak matches the face-center cubic (fcc) NiCo alloy well and is attributed to an equal content of Ni and Co, consistent with the very similar reducibility of those two cations. It is noteworthy that the intensity of peaks corresponding to intergrowth species become weaker for all samples after reduction, suggesting the removal of excess oxygen from the intergrowth species. The ilmenite species also decomposed in the reduction atmosphere with a small amount of rutile produced.

To further understand the influence of dopants on the reducibility of different perovskite fibers, the TGA analysis was performed on calcined fibers in 5% H₂/N₂. The La_{0.52}Ca_{0.28}Ni_{0.04}Fe_{0.04}Ti_{0.92}O₃ fibers start to lose weight at around 580 °C, while this weight loss is delayed to 630 °C for La_{0.52}Ca_{0.28}Ni_{0.03}Co_{0.03}Ti_{0.94}O₃ fibers (Figure 1b). The lost weight amounts to about 0.66% for La_{0.52}Ca_{0.28}Ni_{0.04}Fe_{0.04}Ti_{0.92}O₃, which is higher than for La_{0.52}Ca_{0.28}Ni_{0.03}Co_{0.03}Ti_{0.94}O₃ (0.40%) when the temperature raised to 800 °C. The weight loss values were calculated from 100 °C (the samples were dried at this point for 1 h to maintain a constant weight) to 800 °C to evaluate the relationship between weight loss and temperature. The mass remained constant until 300 °C indicating there is no weight loss during this range. The weight loss of the calcined fibers corresponds typically to the amount of formed oxygen deficiencies:



where O_x[·] and V_o[·] denote oxygen lattice and oxygen deficiency sites, respectively, in perovskite lattices using the Kröger-Vink notation. As the intrinsic reduction occurs with removing oxygen from the lattice, the difference here suggests that the oxygen vacancies formed rapidly in La_{0.52}Ca_{0.28}Ni_{0.04}Fe_{0.04}Ti_{0.92}O₃. The coordination flexibility (multivalency) of Fe may enable greater extent of reduction in titanates.^[30] Moreover, the synergistic effects between Ni and Fe may promote oxygen stripping from the lattice, consistent with a previous report,^[24] which shows that the Fe dopant changes the reduction behavior of Ni-doped La_{0.7}Sr_{0.3}CrO₃ by facilitating the formation of oxygen vacancies. More electrons in the t_{2g}-type d-orbitals of Ni²⁺ relative to iron may increase the electron-donating ability of lone pairs from the bridging oxygen atoms.^[25,35] This enhancement may achieve a more stable environment for high valent ion (Fe⁴⁺) under oxidation condition, thus, more weight loss may be achieved by reduction.

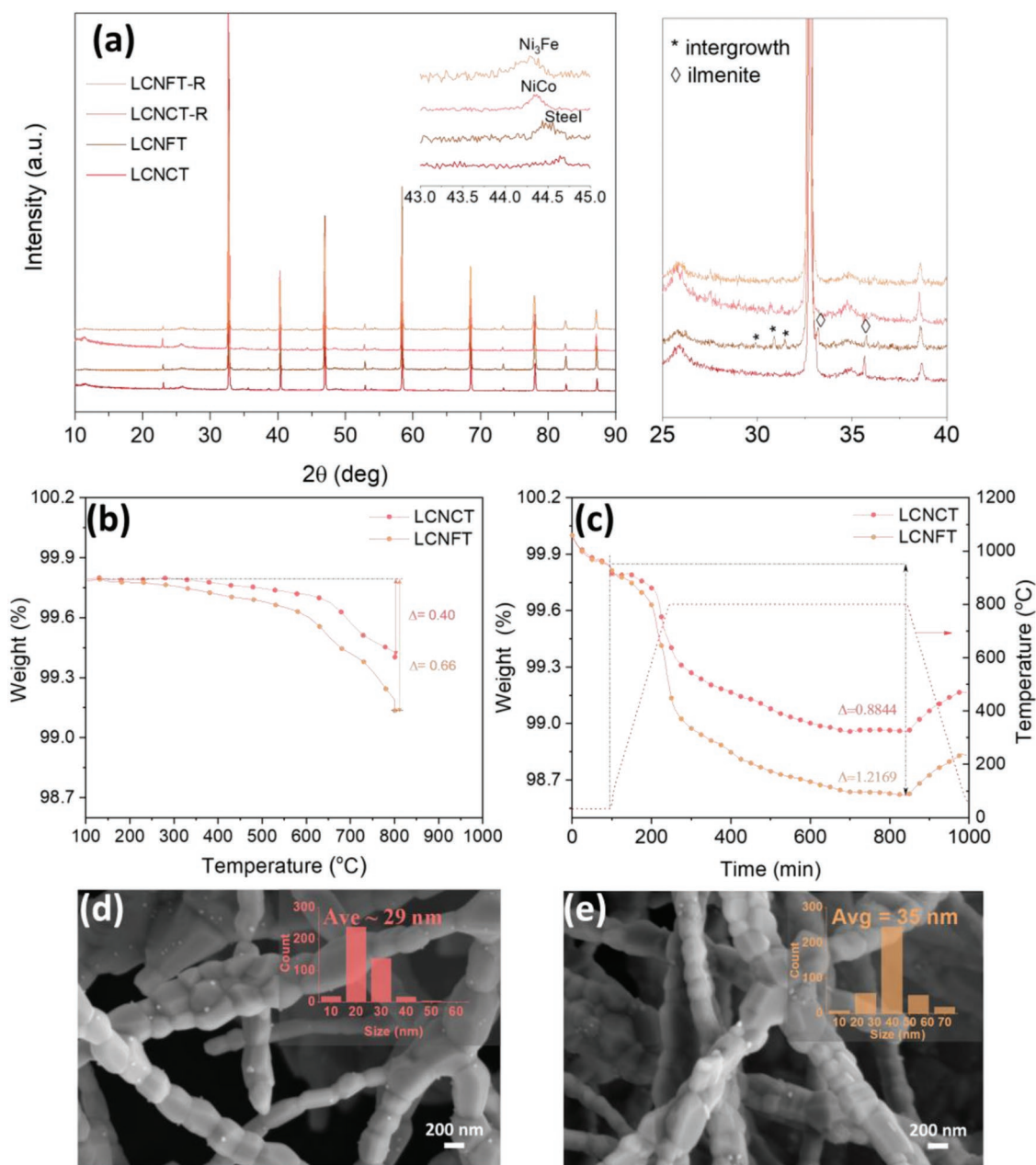


Figure 1. Exsolution of bi-metallic phases from perovskite fiberfibers. a) XRD patterns of Bi-metal doped $\text{La}_{0.52}\text{Ca}_{0.28}\text{Ni}_{0.03}\text{Co}_{0.03}\text{Ti}_{0.94}\text{O}_3$ and $\text{La}_{0.52}\text{Ca}_{0.28}\text{Ni}_{0.04}\text{Fe}_{0.04}\text{Ti}_{0.92}\text{O}_3$ perovskite fiberfibers, the inset shows the reflection between 43 and 45 °. The magnified section of the XRD patterns show the oxygen excess intergrowth and ilmenite species. TGA analysis of fiber samples in 5% H_2/N_2 , b) from 100 to 800 °C, c) from room temperature to 800 °C and isothermal at 800 °C for 10 h. SEM figures of perovskite fiberfibers reduced in 5% H_2/N_2 at 800 °C for 4 h with d) $\text{La}_{0.52}\text{Ca}_{0.28}\text{Ni}_{0.03}\text{Co}_{0.03}\text{Ti}_{0.94}\text{O}_3$, e) $\text{La}_{0.52}\text{Ca}_{0.28}\text{Ni}_{0.04}\text{Fe}_{0.04}\text{Ti}_{0.92}\text{O}_3$.

The fibers were reduced at 800 °C for 10 h until weight loss, i.e., reduction, was complete, as shown in Figure 1c. The weight loss of $\text{La}_{0.52}\text{Ca}_{0.28}\text{Ni}_{0.03}\text{Co}_{0.03}\text{Ti}_{0.94}\text{O}_3$ and $\text{La}_{0.52}\text{Ca}_{0.28}\text{Ni}_{0.04}\text{Fe}_{0.04}\text{Ti}_{0.92}\text{O}_3$ samples reached a plateau in the last 2 h. At the end of the reduction, the weight loss percentage varies for the samples. Oxygen deficiency can be calculated for the samples according to Equation 2:

$$\delta = \frac{M_{\text{ABO}_3} m_{\text{ABO}_3} - m_{\text{ABO}_{3-\delta}}}{M_{\text{O}} m_{\text{ABO}_3}} \quad (2)$$

The oxygen deficiencies produced at the end of the isothermal process are $\delta = 0.099$ and 0.137 for $\text{La}_{0.52}\text{Ca}_{0.28}\text{Ni}_{0.03}\text{Co}_{0.03}\text{Ti}_{0.94}\text{O}_3$ and $\text{La}_{0.52}\text{Ca}_{0.28}\text{Ni}_{0.04}\text{Fe}_{0.04}\text{Ti}_{0.92}\text{O}_3$, respectively. The maximum oxygen deficiencies produced by reducing all B-site doped cations into metallic can be calculated via formula charge neutrality. For example, if about 0.03 atom-% Ni^{2+} and 0.03 atom-% Co^{3+} were doped in B-site of perovskite, then the maximum of oxygen deficiency (assuming no other cations are reduced at this temperature) is 0.075. Similarly, the oxygen deficiency from the reduction of doped cations

for $\text{La}_{0.52}\text{Ca}_{0.28}\text{Ni}_{0.04}\text{Fe}_{0.04}\text{Ti}_{0.92}\text{O}_3$ should be 0.120, therefore, the larger oxygen deficiencies (0.137) seems originated from the reduction of Ti^{4+} . The reduction of titanium cation at high temperatures have been reported in previous works.^[36,37]

The Fe doped samples demonstrate more oxygen deficiencies than $\text{La}_{0.52}\text{Ca}_{0.28}\text{Ni}_{0.03}\text{Co}_{0.03}\text{Ti}_{0.94}\text{O}_3$ after reduction. The higher oxygen deficiency formed in Fe doped samples compared with Ni and Co doped perovskite reveals that the flexibility of oxygen states may boost the formation of oxygen vacancies. It is also plausible to attribute this difference to the oxygen-rich intergrowth regions, as the intergrowth vanished after the reduction (Figure 1a). The intergrowth species were readily reduced due to the locally weaker (stretched) Ti–O bonds and absence of hindering of A-site cations around the intergrowths that causes a high mobility of oxide ions.

The termination of weight loss indicates the end of formation of more oxygen vacancies for the perovskite. Thus, it is possible that the diffusion of B-site doped cations may stop at this stage. As the B-site doped cation migrates to the surface of perovskite, nucleation occurs following reduction. The metallic species continuously grow into nanoparticles at the high temperature. The slow diffusion of B-site cations in $\text{La}_{0.52}\text{Ca}_{0.28}\text{Ni}_{0.03}\text{Co}_{0.03}\text{Ti}_{0.94}\text{O}_3$ may result in a smaller nanoparticle size (Figure 1d,e). Uniform nanoparticles are exsolved from the fiber backbone after reduction, compared with the fiber before (Figure S2, Supporting Information) and after reduction (Figure 1d,e; Figure S3, Supporting Information). The insets show the particle size distribution histogram as measured from SEM images. The fibers are multi-micrometer long and about 200 nm in diameter. The average diameter of exsolved particles are about 29 and 35 nm for $\text{La}_{0.52}\text{Ca}_{0.28}\text{Ni}_{0.03}\text{Co}_{0.03}\text{Ti}_{0.94}\text{O}_3$ and $\text{La}_{0.52}\text{Ca}_{0.28}\text{Ni}_{0.04}\text{Fe}_{0.04}\text{Ti}_{0.92}\text{O}_3$ samples, respectively.

The reduction duration is one of the factors in controlling the exsolved particle size as the diffusion of cations determines the growth of nanoparticles, which is a time-consuming process. The ions continuously segregate on the surface of fibers as the reduction progresses, leading to a growth of nanoparticles (Figure S4, Supporting Information). The nanoparticles on Ni and Co co-doped fibers are approximately 47 nm in size after reduction at 800 °C for 10 h, and this is almost doubled in size compared with the one reduced only for 4 h (about 29 nm) (Figure 1d,e). For the Ni and Fe co-doped samples, nanoparticles appear to grow less steadily with reduction time, increasing from 35 to 48 nm during the same reduction period.

2.2. Electrochemical Performance in SOEC

The electrochemical performance of cells based on bi-metal doped fiber electrodes was measured using an 8YSZ electrolyte (with 200 μm thickness) supported electrolytic cell. The bi-metal doped perovskite fiber slurry and the LSM/YSZ powder slurry were painted on both sides of the electrolyte as fuel and air electrodes, respectively. The LSM/YSZ electrode was fired after the fabrication of the perovskite fiber electrode, both of them are fired at 1100 °C in air.

The impedance results of the cells based on $\text{La}_{0.52}\text{Ca}_{0.28}\text{Ni}_{0.03}\text{Co}_{0.03}\text{Ti}_{0.94}\text{O}_3$ and $\text{La}_{0.52}\text{Ca}_{0.28}\text{Ni}_{0.04}\text{Fe}_{0.04}\text{Ti}_{0.92}\text{O}_3$ fibers as electrolyser at OCV after previous switching at 900 °C

for 180 s in CO_2 (Figure 2a,d). After switching at 1.8 V, the $\text{La}_{0.52}\text{Ca}_{0.28}\text{Ni}_{0.03}\text{Co}_{0.03}\text{Ti}_{0.94}\text{O}_3$ based cell exhibits a polarisation resistance of about 60 Ω cm² at OCV that is much smaller than that of the $\text{La}_{0.52}\text{Ca}_{0.28}\text{Ni}_{0.04}\text{Fe}_{0.04}\text{Ti}_{0.92}\text{O}_3$ based cell (>200 Ω cm²). Upon increasing the switching potential to 2.0 V, both ohmic resistance (R_s) and polarisation resistance (R_p) are significantly enhanced to form a semicircle for $\text{La}_{0.52}\text{Ca}_{0.28}\text{Ni}_{0.03}\text{Co}_{0.03}\text{Ti}_{0.94}\text{O}_3$ but not for the $\text{La}_{0.52}\text{Ca}_{0.28}\text{Ni}_{0.04}\text{Fe}_{0.04}\text{Ti}_{0.92}\text{O}_3$ -based electrolyser. However, all the cells exhibit lower resistance after switching at 2.1 V for 180 s while the R_p for $\text{La}_{0.52}\text{Ca}_{0.28}\text{Ni}_{0.04}\text{Fe}_{0.04}\text{Ti}_{0.92}\text{O}_3$ is still quite significant.

However, a distinct tendency can be seen for the EIS results below 1.35 V (Figure 2b,e). The EIS value at 1.35 V provides practical information of the cell as the electrolyser was measured at 1.35 V in CO_2 . The gas-solid or solid-solid reactions were the dominating processes as the maximum frequency measured changed from 12 to 50 Hz. This middle frequency range between 10–100 Hz indicates that gas adsorption, desorption, and dissociation or surface diffusion and ionic charge transfer are the dominated process in the cells.^[38,39] The R_s of the $\text{La}_{0.52}\text{Ca}_{0.28}\text{Ni}_{0.03}\text{Co}_{0.03}\text{Ti}_{0.94}\text{O}_3$ fiber based cell increased slightly after switching at 1.8 V but reduced when increasing the voltages to 2.0 and 2.1 V. Similar trends can be seen for the R_p value which indicates the electrode is well activated at this high voltage. The R_s value after switching remains identical to the one before switching for cells with $\text{La}_{0.52}\text{Ca}_{0.28}\text{Ni}_{0.04}\text{Fe}_{0.04}\text{Ti}_{0.92}\text{O}_3$ electrodes.

A slightly decreased R_p value occurred for the $\text{La}_{0.52}\text{Ca}_{0.28}\text{Ni}_{0.04}\text{Fe}_{0.04}\text{Ti}_{0.92}\text{O}_3$ fiber based cell after increasing the switching voltage to 2.0 V (Figure 2e). In contrast, the value of R_p decreased by more than factor of two for $\text{La}_{0.52}\text{Ca}_{0.28}\text{Ni}_{0.03}\text{Co}_{0.03}\text{Ti}_{0.94}\text{O}_3$ based cells, namely from 4.63 to 1.97 Ω cm². In particular, after applying a switching voltage of 2.1 V, changes in R_p occurred with calculated value reduced from 4.63 to 1.04 Ω cm² for $\text{La}_{0.52}\text{Ca}_{0.28}\text{Ni}_{0.03}\text{Co}_{0.03}\text{Ti}_{0.94}\text{O}_3$ and from 1.08 to 0.60 Ω cm² for $\text{La}_{0.52}\text{Ca}_{0.28}\text{Ni}_{0.04}\text{Fe}_{0.04}\text{Ti}_{0.92}\text{O}_3$ based cells (Table S2, Supporting Information). The current density decreased under the switching potential (1.8–2.1 V) for 180 s but the end value increased with the switching potential (Figure 2c,f). The current density under the switching potential for $\text{La}_{0.52}\text{Ca}_{0.28}\text{Ni}_{0.03}\text{Co}_{0.03}\text{Ti}_{0.94}\text{O}_3$ based cell is higher than that of the $\text{La}_{0.52}\text{Ca}_{0.28}\text{Ni}_{0.04}\text{Fe}_{0.04}\text{Ti}_{0.92}\text{O}_3$ based cell, which shows a similar tendency with impedance.

The low switching voltage may not be enough for the activation of the electrode (for example, via reduction of Ti^{4+}), however, degradation on cathode^[40] or starvation of active sites may overwhelm than the inferior switching due to increased current.^[41] The decreased R_p values occur after switching at high voltage (>2.0 V) indicating the improved kinetics of gas conversion due to the increasing amount of active sites. According to the switching process, it is reasonable to assumed that the onset of switching and the triggering of exsolution occur when the applied potential exceeds 2.0 V.^[42]

It is worth mentioning that although the $\text{La}_{0.52}\text{Ca}_{0.28}\text{Ni}_{0.03}\text{Co}_{0.03}\text{Ti}_{0.94}\text{O}_3$ electrode displays obvious changes after switching, the R_p value is still inferior to that of $\text{La}_{0.52}\text{Ca}_{0.28}\text{Ni}_{0.04}\text{Fe}_{0.04}\text{Ti}_{0.92}\text{O}_3$ (Table S2, Supporting Information). The electrolysis performance was studied by cells with

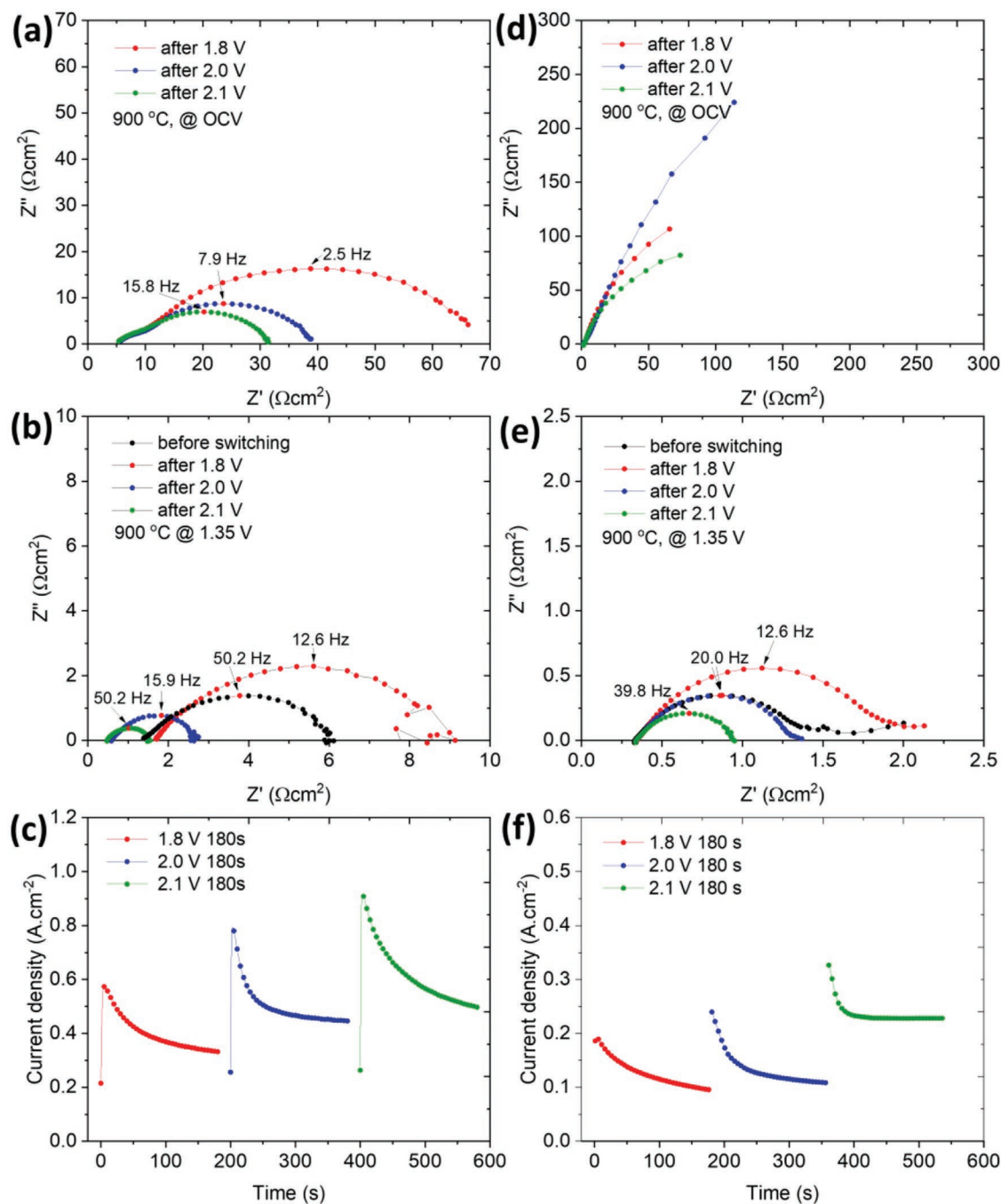


Figure 2. CO₂ electrolyser based on different fiber cathodes with switching at 900 °C in pure CO₂ for 180 s at 1.8 V, 2.0 V and 2.1 V. Impedance spectra of perovskite fiber based cell after switching for La_{0.52}Ca_{0.28}Ni_{0.03}Co_{0.03}Ti_{0.94}O₃ at a) OCV and b) 1.35 V, and La_{0.52}Ca_{0.28}Ni_{0.04}Fe_{0.04}Ti_{0.92}O₃ at d) OCV and e) 1.35 V. The corresponding current density changes versus time during the switching process are showing in c, f) for La_{0.52}Ca_{0.28}Ni_{0.03}Co_{0.03}Ti_{0.94}O₃ and La_{0.52}Ca_{0.28}Ni_{0.04}Fe_{0.04}Ti_{0.92}O₃, respectively.

La_{0.52}Ca_{0.28}Ni_{0.03}Co_{0.03}Ti_{0.94}O₃ and La_{0.52}Ca_{0.28}Ni_{0.04}Fe_{0.04}Ti_{0.92}O₃ fibers in configurations Perovskite fiber(cathode)/YSZ/LSM-YSZ(anode) under applied voltages ranging from 0.2 to 1.6 V at 900 °C in pure CO₂. Typical curves of voltage versus current density of the carbon dioxide electrolyser (Figure 3a). The current-voltage (IV) curve addresses two different processes in the two voltage regions: a) the electrochemical reduction of

the cathodes at low voltages and b) the CO₂ electrolysis at high voltages (ohmic regime, see the fitted straight line). The slopes of both IV curves change at approximately 1.17 and 1.24 V for La_{0.52}Ca_{0.28}Ni_{0.03}Co_{0.03}Ti_{0.94}O₃ and La_{0.52}Ca_{0.28}Ni_{0.04}Fe_{0.04}Ti_{0.92}O₃, respectively. The slopes of the IV curves in the ohmic regime reflect the internal resistances of the cells with values for La_{0.52}Ca_{0.28}Ni_{0.03}Co_{0.03}Ti_{0.94}O₃ and La_{0.52}Ca_{0.28}Ni_{0.04}Fe_{0.04}Ti_{0.92}O₃

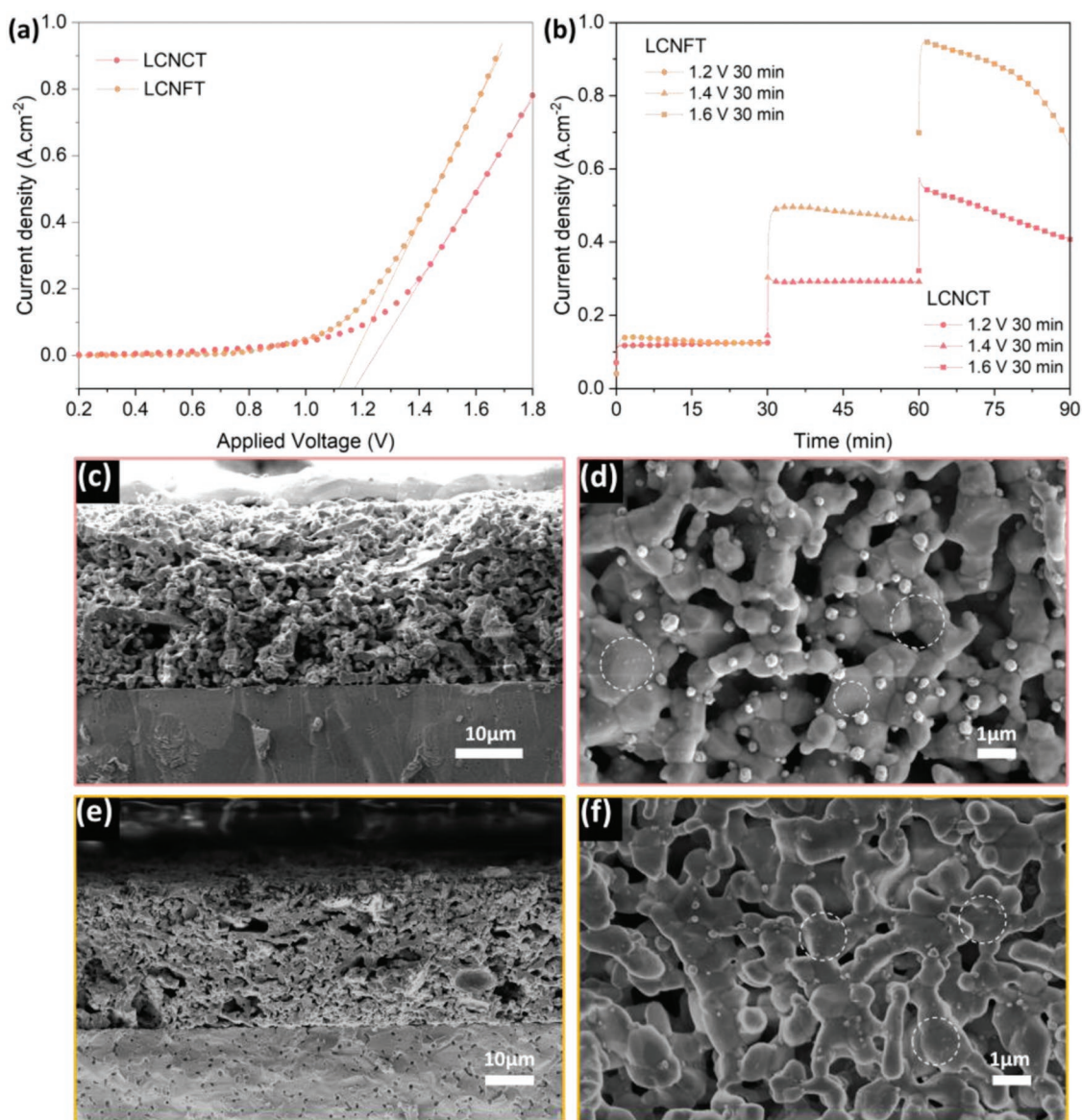


Figure 3. Pure CO₂ electrolyser of perovskite fiber based solid oxide cells. a) Current-Voltage curves of electrolyser cells based La_{0.52}Ca_{0.28}Ni_{0.03}Co_{0.03}Ti_{0.94}O₃ and La_{0.52}Ca_{0.28}Ni_{0.04}Fe_{0.04}Ti_{0.92}O₃ fiber electrodes at 900 °C in CO₂. b) Short-term performance of electrolysing CO₂ based on La_{0.52}Ca_{0.28}Ni_{0.03}Co_{0.03}Ti_{0.94}O₃ and La_{0.52}Ca_{0.28}Ni_{0.04}Fe_{0.04}Ti_{0.92}O₃. SEM image of the fiber cathode for SOEC after CO₂ electrolysis measurement c, d) La_{0.52}Ca_{0.28}Ni_{0.03}Co_{0.03}Ti_{0.94}O₃ and (e, f) La_{0.52}Ca_{0.28}Ni_{0.04}Fe_{0.04}Ti_{0.92}O₃. The exsolved particles are highlighted with white circles.

fiber electrodes of 0.57 Ω and 0.74 Ω cm², respectively. The maximum current density at 1.6 V reaches 0.49 and 0.75 Acm⁻² for LCNCT and La_{0.52}Ca_{0.28}Ni_{0.04}Fe_{0.04}Ti_{0.92}O₃, respectively. The higher currents observed in these cells are consistent with the EIS results at 1.35 V (Figure 2). The performance of those CO₂ electrolyser cells based on two bi-metal doped perovskite fiber electrodes are superior to those with electrodes of similar composition (La_{0.43}Ca_{0.37}Ni_{0.06}Ti_{0.94}O₃ and La_{0.43}Ca_{0.37}Ni_{0.03}Fe_{0.03}Ti_{0.94}O₃) prepared by the solid-state method.^[41] The better performance for our fiber-based oxide cells may be attributed to smaller grain size (higher surface area).

The short term stability was evaluated for the cells with La_{0.52}Ca_{0.28}Ni_{0.04}Fe_{0.04}Ti_{0.92}O₃ and La_{0.52}Ca_{0.28}Ni_{0.03}Co_{0.03}Ti_{0.94}O₃ cathode, electrolysing CO₂ at 1.2, 1.4 and 1.6 V for 30 mins

(Figure 3b). The current densities increase significantly when the potential is increased from 1.2 V to 1.6 V indicating improved CO₂ adsorption and activation performed at high current density. Though the current densities are stable at both 1.2 and 1.4 V, they exhibit a clear decrease when a voltage of 1.6 V is applied. The decreasing current density may due to the unstable of materials at high current density, for example the oxidation of nanoparticles under the potential.^[43] The current density with the La_{0.52}Ca_{0.28}Ni_{0.03}Co_{0.03}Ti_{0.94}O₃ fiber cathode reaches 0.12, 0.29 and 0.54 Acm⁻² at 1.2, 1.4 and 1.6 V, respectively. In contrast, the La_{0.52}Ca_{0.28}Ni_{0.04}Fe_{0.04}Ti_{0.92}O₃ fiber based cell displays a better performance with the current density of 0.20, 0.45 and 0.76 Acm⁻² at 1.2, 1.4 and 1.6 V, respectively. Both cells exhibit higher current densities than cells with (La,Sr)

TiO_{3+δ} and Mn doped (La,Sr)TiO_{3+δ} cathodes (about 0.15 Acm⁻² at 800 °C).^[44] The higher current densities of the fiber electrodes based electrolysis cells illustrate that the Ni and Fe co-doped perovskite are active for CO₂ electrolysis.

The small size of the exsolved nanoparticles should result in higher catalytic activity due to increased surface area. The microstructure of the fiber electrodes after measurement was examined by SEM (Figure 3c,f). The insets present the microstructures of YSZ electrolyte-supported cells based on fabric electrodes. After the electrochemical measurements, the 30 μm thick electrodes maintained their porous structure and adhered well to the YSZ electrolyte. Switching leads to the formation of nanoparticles with an average size of about 40 nm that are maintained after the electrochemical measurement, as highlighted by the white circles (Figure 3d,f). The difference in shape between these nanoparticles and those that are purely Ni may be caused by the presence of Fe as the exsolved Fe nanoparticles display non-spheroid shapes. The larger nanoparticles (100 to 200 nm) with the different contrast are gold particles from the current collector which are not expected to contribute to the activity.^[45]

2.3. Morphology Characterization

The bi-metal doped fibers sintered at 1100 °C in air display a dense structure with distinct and interconnected grains (Figure S2, Supporting Information). The high temperature sinters the fiber into dense grains, without pores forming in the fiber. The densified morphology also leads to a low surface area (Figure S5, Supporting Information). The BET area for the three fiber samples calcined at 1100 °C is similar, with a value of 1.57 and 2.45 m²g⁻¹ for La_{0.52}Ca_{0.28}Ni_{0.03}Co_{0.03}Ti_{0.94}O₃ and La_{0.52}Ca_{0.28}Ni_{0.04}Fe_{0.04}Ti_{0.92}O₃ fibers, respectively. The small surface area is consistent with the figures from SEM indicating dense grains of the perovskite fibers. The fibers show similar morphology with continuous structure and diameters between 200 and 400 nm. The fibers are thick and constructed with many discrete grains present in the fibers rather than having ripened into fewer, larger grains. This may be due to the thermal stability of alloy, which may stabilize nanocrystalline solids against grain-growth compared with single metal phases.^[46] More types of cations present in the electrospinning precursor which lead to a weak chelation between cations and PVP in the precursor, as exact concentration of cations (0.2 M) and PVP (2.5 wt%) in the precursor were used for the all samples.

The cell based on La_{0.52}Ca_{0.28}Ni_{0.04}Fe_{0.04}Ti_{0.92}O₃ fibers demonstrates better performance than that based on La_{0.52}Ca_{0.28}Ni_{0.03}Co_{0.03}Ti_{0.94}O₃, which suggests a superior catalytic activity of exsolved NiFe over NiCo particles. We therefore have inspected the microstructure of the exsolved nanoparticles on La_{0.52}Ca_{0.28}Ni_{0.04}Fe_{0.04}Ti_{0.92}O₃ perovskite fibers in more detail. Herein, the reduced La_{0.52}Ca_{0.28}Ni_{0.04}Fe_{0.04}Ti_{0.92}O₃ sample (denoted as NiFe@LCNFT) was further examined by TEM equipped with EDX and EELS to study the nature of exsolved nanoparticles and understand the process for the formation of oxygen deficiency. The metallic particle on top of the fiber is about 50 nm in diameter, while some small particles are around 20 nm in size, highlighted in the red rectangle

(Figure 4). All elements except nickel and iron are evenly distributed in the fiber.

The composition of nanoparticle (area 1) and the fiber (area 2) was examined by EDX elemental analysis (Figure 4b). The bi-metallic particle with a Ni: Fe ratio about 2.4:1 is close to the previously reported Ni₃Fe alloy particles.^[26,34,47] Though the fibers were reduced for 10 h, some nickel and iron are still retained in the lattice. The bulk exhibits a Ni: Fe ratio of 1:5.2 indicating that Ni and Fe are partially exsolved from the fiber with most of the Fe remaining in the perovskite lattice. The particle shows a six-fold structure (Figure 4c). The different contrast in the dark field STEM image shows the particle has the shape of a decahedron with the facets curved resembling the Wulff polyhedron shape (see the Figure S6, Supporting Information). Commonly, the exsolved metallic particles are homogeneous and epitaxial with respect to the support.^[36] The cell parameter mismatch between the Ni₃Fe particle and the perovskite in c direction is about 7.6% (for La_{0.52}Ca_{0.28}Ni_{0.04}Fe_{0.04}Ti_{0.92}O₃, a = b = 5.474 Å, c = 7.750 Å (Table S1, Supporting Information), and the Ni₃Fe cubic cell parameter is a = 3.582 Å^[48]). To accommodate the mismatch between metal lattice and perovskite and reduce the surface energy, the exsolved nanoparticles have the prone to form into an irregular shapes.^[49]

Two more exsolved particles were characterized by TEM (Figure S7). The particles are ellipsoidal, with about a third submerged into the parent oxide. The EDX mappings show that La, Ca, Ti and O are distributed only in the perovskite bulk, while the nanoparticles consist of only Fe and Ni. The quantitative result from EDX spectra shows similar Ni: Fe ratio in those alloy particle about 2.7:1 (Figure 4). The composition of the bulk area is La_{0.51}Ca_{0.21}Ni_{0.004}Fe_{0.012}Ti_{0.92} which exhibits a close ratio for La, Ca, Ti with the devised stoichiometry (La_{0.52}Ca_{0.28}Ti_{0.92}) but three times more Fe than Ni. From the amount of metals left in the bulk of the reduced sample it can be concluded that most of the Ni (about 90%) is exsolved and about 30% of Fe remains in the material.

The result of EELS can also confirm the metallic property of the nanoparticle. Measurements of iron valence ratios (Fe³⁺/ΣFe) in the material can provide valuable information of past redox states.^[50] The nano-scale resolution of STEM/EELS provides information of the Fe³⁺/ΣFe ratio that is deduced from the indicative value of white line ratio, L₃/L₂. This ratio is obtained from the background-subtracted and Fourier ratio deconvolved spectrum by integrating two narrow energy windows, 2 eV in width (Figure S7c, Supporting Information). The core loss spectra are aligned to the center of the Fe L₂ and L₃ peaks in the energy window. The distance between the two peaks is about 12.9 eV. Here, integrated from the spectra, the value of L₃/L₂ was calculated as 2.27(5) indicating a zero oxidation state compare with previous work.^[50] The Ni L₃ position locates at 852.2 eV also indicating the metallic state of Ni in the particle.^[51]

The oxidation states of titanium in the bulk, the near surface of exsolved particle and overlayer regions were investigated in selected areas (Figure 5). The particle is socketed into the perovskite with epitaxial growth aligning with the (110) plane (Figure 5b). The metal lattice growing from the perovskite lattice might naturally facilitate interdiffusion between the two, which results in the socketed structure. It should be noted that

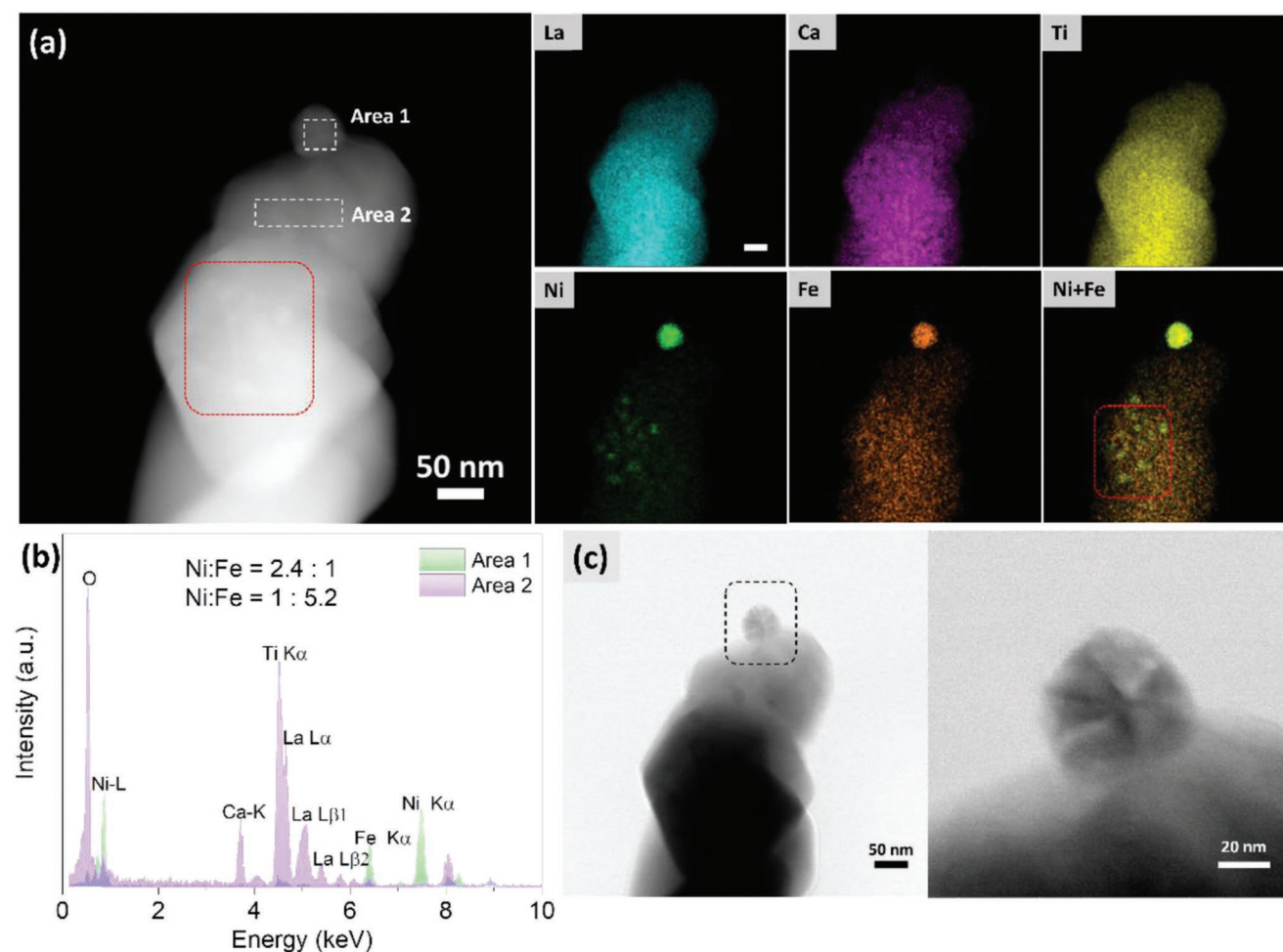


Figure 4. Microstructural of reduced $\text{La}_{0.52}\text{Ca}_{0.28}\text{Ni}_{0.04}\text{Fe}_{0.04}\text{Ti}_{0.92}\text{O}_3$ fibers. a) TEM image of NiFe@LCNFT fiber and corresponding EDX mapping, b) EDX analysis of the area indicated in HAADF image, c) HRTEM image of the nanoparticles in dark field model.

the d-spacing of metallic particles and the perovskite are 2.7 and 3.0 Å, respectively. The mismatch (10%) may cause dislocation and strain in the metal lattice.

Moreover, an overlayer (labeled as area ③ in Figure 5c) formed on the ridge of the exsolved particle. The fast Fourier transform (FFT) pattern and the lattice reveals that the wrapped area has a similar atomic arrangement as the host perovskite (Figure 5d). However, the EDX counting statistics data indicates the wrapped area displays a different elemental composition compared to the support (Figure 5d). The La:Ca:Ti ratio is 0.35:0.18:1 which indicates a titanium enriched composition compared to the $\text{La}_{0.52}\text{Ca}_{0.28}\text{Ni}_{0.04}\text{Fe}_{0.04}\text{Ti}_{0.92}\text{O}_3$ perovskite. Similar appendage (as-grown oxide, La_2TiO_5) was also observed by reducing the $\text{La}_{0.8}\text{Ce}_{0.1}\text{Ni}_{0.4}\text{Ti}_{0.6}\text{O}_{3-\delta}$ perovskite at 1000 °C for 10 h.^[52]

To understand the mechanism of the formation of these wrapped phases, different areas (①, ② and ③ marked in the HR-STEM) were examined by EELS on titanium. The EELS spectrum indicate the reduction of titanium in this overlap area (Figure 5f). The near-surface, bulk and the overlayer regions all reveal clear Ti $L_{3,2}$ -edge signals. The splitting of L_3 and L_2 doublets is related to the change of valence state and coordination

number of titanium. The spectral fitting and position were analysed to reveal Ti species in three selected areas.^[53] The spectra of perovskite bulk area ① exhibits a typical profile for the Ti^{4+} phase with clear crystal field splitting.

The near surface area ② shows similar spectra but a slight shift to lower energy loss. The shift from high to low energy indicates a decrease in the oxidation state of titanium.^[53] The difference between the bulk and the surface may contribute to the sufficient contact with the reduced atmosphere. The 5% H_2/N_2 used here to drive the exsolution of metallic nanoparticles also reduces the titanium in perovskite. As for the overlayer coated on the nanoparticles, clear Ti^{3+} characteristics appear in the EELS spectra indicating the presence of phases with reduced Ti. The difference between host surface area ② and the overlayer ③ reveals that the titanium atoms in the overlayer are reduced to a higher extent than on the surface. Thus, the presence of metallic nanoparticles, expected to promote charge transfer, may facilitate the reduction of the host oxides. This in turn produces more reduced host phases and coated on the nanoparticles finally. Similar structures have been reported on Ni exsolved system where the formation of such overlayers was suggested to enhance the stability of the material.^[12] The

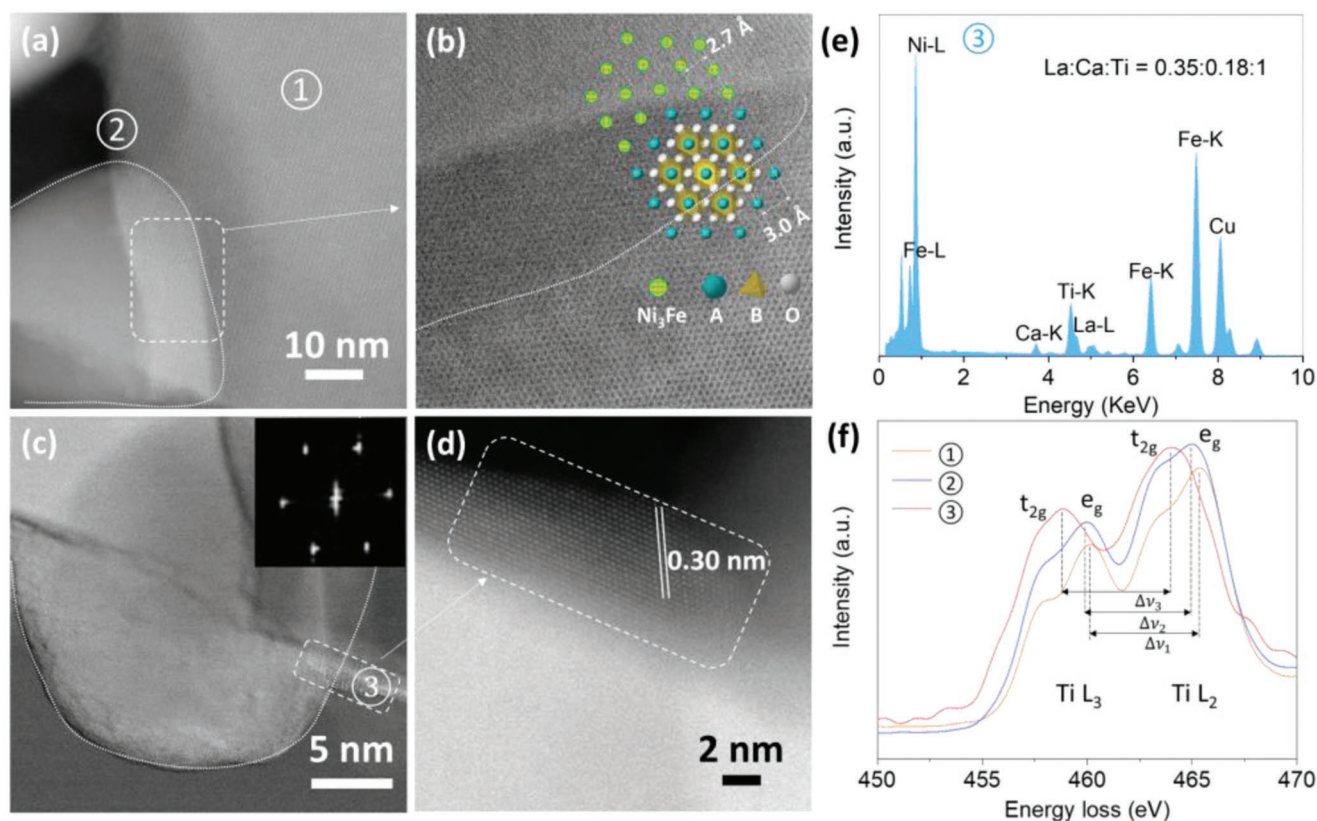


Figure 5. Exsolved particle-substrate interface. a) STEM image of the selected area for NiFe@LCNFT fiber. Areas ① and ② are the bulk and the surface region, respectively. b) The interface between particle and the perovskite. The schematic atomic model is shown as inset. c) STEM image highlighting the wrapped area ③ and the corresponding FFT. d) HR-STEM of the wrap area ③. e) EDX analysis of the area ③ indicated in the HAADF figure d). f) EELS spectra for Ti $L_{2,3}$ edge corresponding to areas ①, ② and ③. The used EELS spectra were background-subtracted.

reduction of the titanates contributes to the higher extent of reduction for $\text{La}_{0.52}\text{Ca}_{0.28}\text{Ni}_{0.04}\text{Fe}_{0.04}\text{Ti}_{0.92}\text{O}_3$ fibers as shown in the TGA results (Figure 1c).

2.4. The Role of Fe in the Perovskite Fiber Based Pure CO_2 Electrolyser

As similar morphology and microstructure can be seen for both cells in Figure 3c,f. Thus, the higher CO_2 electrolysis performance of the cell with a $\text{La}_{0.52}\text{Ca}_{0.28}\text{Ni}_{0.04}\text{Fe}_{0.04}\text{Ti}_{0.92}\text{O}_3$ cathode than that with $\text{La}_{0.52}\text{Ca}_{0.28}\text{Ni}_{0.03}\text{Co}_{0.03}\text{Ti}_{0.94}\text{O}_3$ is probably due to the presence of Fe. Considering the lower catalytic activity of $\text{La}_{0.52}\text{Ca}_{0.28}\text{Ni}_{0.04}\text{Fe}_{0.04}\text{Ti}_{0.92}\text{O}_3$ under OCV (Figure 2), the possible effect of Fe may be linked to the increased number of oxygen vacancies, consistent with the TGA results (Figure 1). An improved CO_2 electrolysis performance due to more oxygen vacancies has been reported in the literature and has been ascribed to the promoted adsorption of nonpolar CO_2 on the material surface.^[54] We note that no carbon deposition was observed from the microscopy image, which appears to be another beneficial property of the bi-metallic alloy. It has been reported that under oxidation conditions Fe partially segregates from the alloy forming FeO_x during the reaction. FeO_x can reduce carbon accumulation (through interaction with lattice oxygen),^[55] because carbon fragments deposited on the based

bi-metallic nanoparticles tend to be oxidized to CO rather than coking on the surface.^[17]

The CO_2 conversion on FeNi exsolved perovskite fibers was schematically shown in Figure 6a. The molecular CO_2 gas is adsorbed on the interface between nanoparticles and perovskite fiber first and then converted into CO and oxygen, which upon reduction to oxide ion is incorporated into the anode side from the electrolyte. Quantum-chemical calculations (PBE-D3 level of DFT) were performed to understand the mechanism for CO_2 electrolysis on the CaTiO_3 surface in conjunction with exsolved metal-alloy nanoparticles and oxygen vacancies. We studied the CO_2 adsorption and activation over different surfaces, namely CTO^* , $\text{Fe}_3\text{Ni}_9@ \text{CTO}^*$ and $\text{Ni}_6\text{Co}_6@ \text{CTO}^*$ (where CTO^* denotes a CaTiO_3 surface with one oxygen vacancy). We first studied the reaction pathway of the CO_2 reduction reaction on a pure CTO^* surface with one oxygen vacancy (Figure S8, Supporting Information). The computed adsorption energy is only -0.11 eV (Figure 6b), indicating there is weak physisorption between CO_2 and CTO^* . In contrast, the calculated adsorption energies of CO_2 over $\text{Fe}_3\text{Ni}_9@ \text{CTO}^*$ and $\text{Ni}_6\text{Co}_6@ \text{CTO}^*$ interfaces are -2.84 and -1.79 eV, respectively, indicating strong chemisorption. The larger CO_2 adsorption energy in $\text{Fe}_3\text{Ni}_9@ \text{CTO}^*$ as compared to the Ni_6Co_6 form indicates a better CO_2 adsorption ability of the former.

CO_2 is firmly adsorbed at the interface between the bi-metallic cluster and perovskite (Figure 6c; Figure S9,

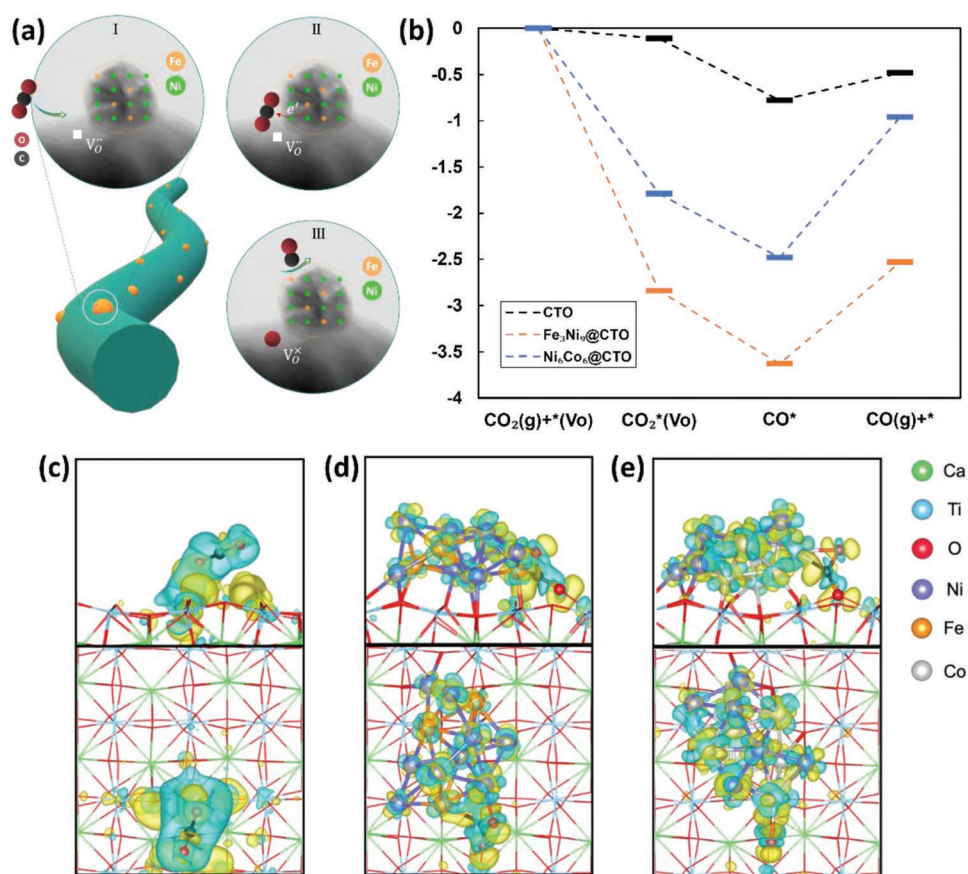


Figure 6. CO₂ conversion over exsolved particles supported on perovskites. a) The processes of CO₂ conversion on perovskite fiber with exsolved active nanoparticles. b) Energy diagrams for CO₂ electrolysis over CaTiO₃ surface, Fe₃Ni₉@CTO interface and Ni₆Co₆@CTO interface, where Vo denotes the oxygen vacancy, CO₂* and CO* refer to intermediates. Charge density difference iso-surface of CO₂ on c) CTO* surface, d) Fe₃Ni₉@CTO* interface and e) Ni₆Co₆@CTO* interface. The yellow and green areas refer to increased and decreased electron densities.

Supporting Information). In both Fe₃Ni₉@CTO* and Ni₆Co₆@CTO* interfaces, the CO₂ form side-on bridging configurations, where the carbon atom and one oxygen atom are bonded to metal nanoparticles and the other oxygen atom is filling up the oxygen vacancy at the CTO* surface (Figure S9,S10, Supporting Information). The strong binding energies between CO₂ and the nanoparticle/CTO* interfaces confirms that the exsolved bi-metallic nanoparticles can improve CO₂ adsorption. The electronic structures of CO₂ adsorbed on different interfaces (Figure 6d). For the Fe₃Ni₉@CTO* interface, the Fe atom donates electrons to the C atom forming the Fe-C contact, while one O atom from CO₂ is bound to a neighboring Ni atom. In the case of the Ni₆Co₆@CTO* interface, the Co atom also donates electrons to the C atom, forming bonds with both C atom and O atom. According to Bader population analysis,^[56] the bare CTO* surface transfers a charge of only 0.02 *e* to the CO₂ molecule, while CO₂ receives 1.22 and 1.12 *e* from Fe₃Ni₉@CTO* and Ni₆Co₆@CTO* interfaces, respectively. Therefore, Fe₃Ni₉@CTO* and Ni₆Co₆@CTO* interfaces show enhanced CO₂ adsorption performance compared to the bare CTO* surface. The products of CO₂ activation are modeled via the resulting CO adsorbed on different interfaces, where the oxygen vacancy has been filled with the other O atom from CO₂ (Figure S8–S10, Supporting Information). According to

the energy profiles, the structures with CO adsorbed on CTO, Fe₃Ni₉@CTO and Ni₆Co₆@CTO have lower energies than the precursors with adsorbed CO₂ on CTO*, with energy differences of –0.67, –0.79 and –0.69 eV, respectively (Figure 6b). Thus, the formation of CO is thermodynamically favorable. The calculated binding energy between CO and CaTiO₃ is only –0.30 eV, indicating a weak physisorption. However, the binding energies of CO are –1.10 and –1.52 eV for Fe₃Ni₉@CTO and Ni₆Co₆@CTO, respectively, indicating a strong chemisorption. From these binding energies it appears that Fe₃Ni₉@CTO is more likely to lose the adsorbed CO molecule than Ni₆Co₆@CTO. The calculation results indicate that exsolved bi-metallic nanoparticles on a CaTiO₃ surface should exhibit enhanced CO₂ catalysis performance compared to bare CaTiO₃, and that the Fe₃Ni₉@CTO interface shows an even better performance than Ni₆Co₆@CTO, consistent with the experimental findings discussed above.

3. Conclusions

The exsolution of bi-metallic nanoparticles from doped perovskites under reductive conditions involves the formation of oxygen vacancies. This work investigated the exsolution

process and morphology for NiCo, and NiFe co-doped perovskite fibers. NiFe co-doped fibers exhibit a faster formation and a higher number of oxygen deficiencies than NiCo doped fibers. The Ni₃Fe particles exsolved on the La_{0.52}Ca_{0.28}Ni_{0.04}Fe_{0.04}Ti_{0.92}O₃ fiber by electrochemical switching facilitate the reduction of titanium from the parent perovskite, leading to a coated overlayer formation. The La_{0.52}Ca_{0.28}Ni_{0.04}Fe_{0.04}Ti_{0.92}O₃ fiber based SOEC shows better performance in CO₂ electrolysis compared with La_{0.52}Ca_{0.28}Ni_{0.03}Co_{0.03}Ti_{0.94}O₃, which is attributed to the synergistic effect of iron. Based on DFT calculations for small bi-metallic nanocluster models on a CaTiO₃ surface, clusters containing Fe shows a stronger interaction with CO₂ and a weaker binding of the product, CO. Overall, our results demonstrate that electrodes based on co-doped perovskite fibers shows great promise for electrocatalysis and have the potential for outperforming solid state powder electrodes.

Supporting Information

Supporting Information is available from the Wiley Online Library or from the author.

Acknowledgements

The authors thank the EPSRC for a Critical Mass project EP/R023522/1 and Electron Microscopy provision EP/R023751/1, EP/L017008/1; The authors also acknowledge support from China Scholarship Council (No. 201706070126). All DFT calculations in this work were performed on the Cirrus UK National Tier-2 HPC Service at EPCC in Edinburgh.

Conflict of Interest

The authors declare no conflict of interest.

Data Availability Statement

The data that support the findings of this study are openly available in PURE at <https://doi.org/10.17630/696452fe-aaf9-4303-8933-0a73e03cbe2b>, reference number [1]. The data that support the findings of this study are available from the corresponding author upon reasonable request.

Keywords

CO₂ electrolysis, electrochemical activation, exsolution, fiber, perovskite

Received: July 30, 2022
Revised: October 7, 2022
Published online:

- [1] M. T. Dunstan, F. Donat, A. H. Bork, C. P. Grey, C. R. Muller, *Chem. Rev.* **2021**, *121*, 12681.
[2] O. S. Bushuyev, P. De Luna, C. T. Dinh, L. Tao, G. Saur, J. van de Lagemaat, S. O. Kelley, E. H. Sargent, *Joule* **2018**, *2*, 825.

- [3] Y. Zheng, J. Wang, B. Yu, W. Zhang, J. Chen, J. Qiao, J. Zhang, *Chem. Soc. Rev.* **2017**, *46*, 1427.
[4] L. Ye, K. Xie, *J. Energy Chem* **2021**, *54*, 736.
[5] M. Pidburtnyi, B. Zanca, C. Coppex, S. Jimenez-Villegas, V. Thangadurai, *Chem. Mater.* **2021**, *33*, 4249.
[6] Y. Tian, Y. Liu, A. Naden, L. Jia, M. Xu, W. Cui, B. Chi, J. Pu, J. T. S. Irvine, J. Li, *J. Mater. Chem. A* **2020**, *8*, 14895.
[7] Y. Gao, C. Xing, S. Hu, S. Zhang, *J. Mater. Chem. A* **2021**, *9*, 10374.
[8] Y. Chen, H. Li, J. Wang, Y. Du, S. Xi, Y. Sun, M. Sherburne, J. W. Ager3rd, A. C. Fisher, Z. J. Xu, *Nat. Commun.* **2019**, *10*, 572.
[9] M. Kothari, Y. Jeon, D. N. Miller, A. E. Pascui, J. Kilmartin, D. Wails, S. Ramos, A. Chadwick, J. T. S. Irvine, *Nat. Chem.* **2021**, *13*, 677.
[10] T. Cao, O. Kwon, R. J. Gorte, J. M. Vohs, *Nanomaterials* **2020**, *10*, 2445.
[11] D. Neagu, G. Tsekouras, D. N. Miller, H. Menard, J. T. S. Irvine, *Nat. Chem.* **2013**, *5*, 916.
[12] S. He, M. Li, J. Hui, X. Yue, *Appl. Catal. B* **2021**, *298*, 120588.
[13] J. H. Kim, J. K. Kim, J. Liu, A. Curcio, J. S. Jang, I. D. Kim, F. Ciucci, W. Jung, *ACS Nano* **2020**, *15*, 81.
[14] B. A. Rosen, *Electrochem* **2020**, *1*, 32.
[15] K. Kim, B. Koo, Y.-R. Jo, S. Lee, J. K. Kim, B.-J. Kim, W. Jung, J. W. Han, *Energy Environ. Sci.* **2020**, *13*, 3404.
[16] Y. Li, K. Xie, S. Chen, H. Li, Y. Zhang, Y. Wu, *Electrochim. Acta* **2015**, *153*, 325.
[17] C. Yang, Z. Yang, C. Jin, G. Xiao, F. Chen, M. Han, *Adv. Mater.* **2012**, *24*, 1439.
[18] K.-Y. Lai, A. Manthiram, *Chem. Mater.* **2018**, *30*, 2838.
[19] Z. Du, H. Zhao, S. Yi, Q. Xia, Y. Gong, Y. Zhang, X. Cheng, Y. Li, L. Gu, K. Swierczek, *ACS Nano* **2016**, *10*, 8660.
[20] T. Zhu, H. E. Troiani, L. V. Mogni, M. Han, S. A. Barnett, *Joule* **2018**, *2*, 478.
[21] S. Song, J. Zhou, X. Su, Y. Wang, J. Li, L. Zhang, G. Xiao, C. Guan, R. Liu, S. Chen, H.-J. Lin, S. Zhang, J.-Q. Wang, *Energy Environ. Sci.* **2018**, *11*, 2945.
[22] V. A. de la Peña O'Shea, M. C. Álvarez-Galván, J. M. Campos-Martín, J. J. L. G. Fierro, *Appl. Catal. A* **2007**, *326*, 65.
[23] R. Thalinger, M. Gocyla, M. Heggen, R. Dunin-Borkowski, M. Grünbacher, M. Stöger-Pollach, D. Schmidmair, B. Klötzer, S. Penner, *J. Catal.* **2016**, *337*, 26.
[24] Y. F. Sun, J. H. Li, L. Cui, B. Hua, S. H. Cui, J. Li, J. L. Luo, *Nanoscale* **2015**, *7*, 11173.
[25] J. Y. Chen, L. Dang, H. Liang, W. Bi, J. B. Gerken, S. Jin, E. E. Alp, S. S. Stahl, *J. Am. Chem. Soc.* **2015**, *137*, 15090.
[26] S. Liu, Q. Liu, J.-L. Luo, *ACS Catal.* **2016**, *6*, 6219.
[27] S. Ding, M. Li, W. Pang, B. Hua, N. Duan, Y.-Q. Zhang, S.-N. Zhang, Z. Jin, J.-L. Luo, *Electrochim. Acta* **2020**, *335*.
[28] J. Zhou, J. Yang, Z. Zong, L. Fu, Z. Lian, C. Ni, J. Wang, Y. Wan, K. Wu, *J. Power Sources* **2020**, *468*, 228349.
[29] B. Hua, M. Li, Y.-F. Sun, Y.-Q. Zhang, N. Yan, J. Chen, T. Thundat, J. Li, J.-L. Luo, *Nano Energy* **2017**, *32*, 247.
[30] N. Dragos, *PhD Doctor of Philosophy*, University of St Andrews, St Andrews **2013**.
[31] J. Canales-Vázquez, J. T. S. Irvine, W. Zhou, *J. Solid State Chem.* **2004**, *177*, 2039.
[32] K. T. Jacob, V. S. Saji, S. N. S. Reddy, *Zh. Khim. Termodin. Termokhim.* **2007**, *39*, 230.
[33] G. Cacciamani, J. De Keyser, R. Ferro, U. E. Klotz, J. Lacaze, P. Wollants, *Intermetallics* **2006**, *14*, 1312.
[34] H. Lv, L. Lin, X. Zhang, D. Gao, Y. Song, Y. Zhou, Q. Liu, G. Wang, X. Bao, *J. Mater. Chem. A* **2019**, *7*, 11967.
[35] J. Hwang, R. R. Rao, L. Giordano, Y. Katayama, Y. Yu, Y. Shao-Horn, *Science* **2017**, *358*, 751.
[36] D. Neagu, T. S. Oh, D. N. Miller, H. Menard, S. M. Bukhari, S. R. Gamble, R. J. Gorte, J. M. Vohs, J. T. S. Irvine, *Nat. Commun.* **2015**, *6*, 8120.

- [37] H. Han, J. Park, S. Y. Nam, K. J. Kim, G. M. Choi, S. S. P. Parkin, H. M. Jang, J. T. S. Irvine, *Nat. Commun.* **2019**, *10*, 1471.
- [38] S. Primdahl, M. Mogensen, *J. Electrochem. Soc.* **1999**, *146*, 2827.
- [39] S. Jo, H. G. Jeong, Y. H. Kim, D. Neagu, J.-h. Myung, *Appl. Catal. B* **2021**, *285*, 119828.
- [40] K. Yasumoto, M. Shiono, H. Tagawa, M. Dokiya, K. Hirano, J. Mizusaki, *J. Electrochem. Soc.* **2002**, *149*, A531.
- [41] M. Chanthanumataporn, J. Hui, X. Yue, K. Kakinuma, J. T. S. Irvine, K. Hanamura, *Electrochim. Acta* **2019**, *306*, 159.
- [42] A. K. Opitz, A. Nenning, V. Vonk, S. Volkov, F. Bertram, H. Summerer, S. Schwarz, A. Steiger-Thirsfeld, J. Bernardi, A. Stierle, J. Fleig, *Nat. Commun.* **2020**, *11*, 4801.
- [43] Y. Song, Z. Zhou, X. Zhang, Y. Zhou, H. Gong, H. Lv, Q. Liu, G. Wang, X. Bao, *J. Mater. Chem. A* **2018**, *6*, 13661.
- [44] W. Qi, Y. Gan, D. Yin, Z. Li, G. Wu, K. Xie, Y. Wu, *J. Mater. Chem. A* **2014**, *2*, 6904.
- [45] M. Guillodo, P. Vernoux, J. Fouletier, *Solid State Ionics* **2010**, *1*, 99.
- [46] J. Weissmüller, *Nanostruct. Mater.* **1993**, *3*, 261.
- [47] D. Papargyriou, D. N. Miller, J. T. S. Irvine, *J. Mater. Chem. A* **2019**, *7*, 15812.
- [48] R. J. Wakelin, E. L. Yates, *Proc. Phys. Soc., London, Sect. B* **1953**, *66*, 221.
- [49] C. R. Henry, *Prog. Surf. Sci.* **2005**, *80*, 92.
- [50] H. Tan, J. Verbeeck, A. Abakumov, G. Van Tendeloo, *Ultramicroscopy* **2012**, *116*, 24.
- [51] J. Fink, T. Muller-Heinzerling, B. Scheerer, W. Speier, F. U. Hillebrecht, J. C. Fuggle, J. Zaanen, G. A. Sawatzky, *Phys. Rev. B* **1985**, *32*, 4899.
- [52] D. Neagu, V. Kyriakou, I. L. Roiban, M. Aouine, C. Tang, A. Caravaca, K. Kousi, I. Schreur-Piet, I. S. Metcalfe, P. Vernoux, M. C. M. van de Sanden, M. N. Tsampas, *ACS Nano* **2019**, *13*, 12996.
- [53] E. Stoyanov, F. Langenhorst, G. Steinle-Neumann, *Am. Mineral.* **2007**, *92*, 577.
- [54] H. Lv, T. Liu, X. Zhang, Y. Song, H. Matsumoto, N. Ta, C. Zeng, G. Wang, X. Bao, *Angew. Chem. Int. Ed.* **2020**, *59*, 15968.
- [55] S. A. Theofanidis, V. V. Galvita, H. Poelman, G. B. Marin, *ACS Catal.* **2015**, *5*, 3028.
- [56] W. Tang, E. Sanville, G. Henkelman, *J. Phys.: Condens. Matter* **2009**, *21*, 084204.